Powder Technology 254 (2014) 30–35

Contents lists available at ScienceDirect

Powder Technology

journal homepage: www.elsevier.com/locate/powtec

Surfactant-free solvothermal synthesis and optical characterization of $Bi_2Fe_4O_9$ in mixed H_2O/EtOH solvent

Yi Liu [a,b], Ruzhong Zuo [a,*], Shishun Qi [a]

[a] Institute of Electro Ceramics & Devices, School of Materials Science and Engineering, Hefei University of Technology, Hefei, 230009, PR China
[b] School of Physics and Electronic Information, Huaibei Normal University, Huaibei, 235000, PR China

ARTICLE INFO

Article history:
Received 21 August 2013
Received in revised form 26 November 2013
Accepted 6 January 2014
Available online 12 January 2014

Keywords:
Hydrothermal synthesis
Crystal growth
$Bi_2Fe_4O_9$ crystals
Optical property
Photocatalyst

ABSTRACT

$Bi_2Fe_4O_9$ powders with different morphology and particle size have been prepared via surfactant-free solvothermal route with water and water–ethanol mixed solvents. The as-synthesized samples were characterized by powder X-ray diffraction, scanning electron microscopy, Fourier transform infrared spectroscopy and UV–vis spectroscopy. The effect of the solvent on the morphology of $Bi_2Fe_4O_9$ crystals and the formation process of rod-like microrods and defective crystals were investigated. Rod-like and cubic shape $Bi_2Fe_4O_9$ crystals could be easily obtained by changing the volume ratios of H_2O/EtOH. The results indicate that the rod-like $Bi_2Fe_4O_9$ crystals could be formed in the more ionic solvent, and the anisotropic nature of the crystal structure may be responsible for the formation of rod-shape. In addition, the optical properties and photocatalytic activity of the $Bi_2Fe_4O_9$ samples were investigated. The lower photocatalytic activity of $Bi_2Fe_4O_9$ microrods could be attributed to their larger particle size, smaller specific surface areas and smaller bandgap.

© 2014 Elsevier B.V. All rights reserved.

1. Introduction

Bismuth ferrites have attracted extensive interests in recent years for their potential applications in sensing, actuation, and digital memory [1–3]. As a typical bismuth ferrite, $Bi_2Fe_4O_9$ has an orthorhombic crystal structure with a space group Pbam. Bulk $Bi_2Fe_4O_9$ ceramics exhibited an antiferromagnetic ordering (T_N ~ 260 K) and ferroelectric hysteresis at T = 250 K, demonstrating that $Bi_2Fe_4O_9$ is one of the promising multiferroic materials [4]. Moreover, $Bi_2Fe_4O_9$ is a multiband semiconductor with high sensitivity to ethanol and acetone vapors [3], which shows potential application as semiconductor gas sensor. Owing to its small bandgap near the range of visible light and UV as well as the ability to photodegrade methyl (MO) [5], phenol, and aqueous ammonia [6], $Bi_2Fe_4O_9$ is also well-known to be an important photocatalytic material. In addition, the catalytic property of the $Bi_2Fe_4O_9$ powder especially concerning the ammonia oxidation to NO is of current interest, because it is likely to replace the high-cost and irrecoverable catalysts based on platinum, rhodium, and palladium in the industrial process of manufacturing nitric acid [7].

It is believed that the properties of functional materials are not only influenced by their chemical compositions and phase structure, but also associate with their microstructure, morphology, dimension and size. Currently, various methods have been developed for the synthesis of $Bi_2Fe_4O_9$ powders with different morphology, such as the sol–gel route [8], molten salt method [9] and hydrothermal process [6,10–13]. However, a high reaction temperature (>700 °C) was needed for both sol–gel and molten salt method. From a practical viewpoint, hydrothermal method is one of the most promising techniques for the synthesis of $Bi_2Fe_4O_9$ powders with regular morphology and homogeneous chemical compositions under milder conditions, because it is usually simpler, energy-efficient, and environment-friendly [14]. The morphology of $Bi_2Fe_4O_9$ has been reported to vary from sheets, plates, to cubes by changing the concentration of NaOH mineralizer, and rode- and fiber-like morphologies could be obtained by adding polyvinyl alcohol as the surfactant [11]. Han et al. prepared smaller $Bi_2Fe_4O_9$ particles with more regular and uniform morphology by increasing the hydrothermal treatment temperature [12]. Du et al. synthesized $Bi_2Fe_4O_9$ nanoplates by using water, while $Bi_2Fe_4O_9$ particles by using the N,N-dimethylformamide as solvent [13]. These previous studies demonstrated that the treatment condition, additive and solvent in the hydrothermal process significantly influence the morphology and particle size of the as-prepared materials. However, the solvothermal method has been rarely adopted to synthesize $Bi_2Fe_4O_9$ crystallites. As far as we know, there has been no report on the solvothermal synthesis of pure $Bi_2Fe_4O_9$ powders by using a mixed solvent of water and ethanol.

It is believed that solvent properties (viscosity, diffusivity, thermal conductivity, dielectric constant, etc.) can influence the diffusion, reactivity, and solubility behavior of the reagents, and therefore play an important role in the crystal growth [15]. Thereby the controlled formation of samples with various morphology or properties was available by varying the volume ratios of mixed-solvent, which has

* Corresponding author. Tel./fax: +86 551 62905285.
E-mail address: piezolab@hfut.edu.cn (R. Zuo).

0032-5910/$ – see front matter © 2014 Elsevier B.V. All rights reserved.
http://dx.doi.org/10.1016/j.powtec.2014.01.013

been reported in the literature [16,17]. The purpose of this work is to tune the morphology and particle size of $Bi_2Fe_4O_9$ powders by using this surfactant-free solvothermal route. The influence of the solvent on the morphology of $Bi_2Fe_4O_9$ crystals was investigated. The optical properties and photocatalytic activity of $Bi_2Fe_4O_9$ samples were characterized as well.

2. Experiments

All reagents were analytical grade and used without further purification. First, 1.0 mmol $Bi(NO_3)_3 \cdot 5H_2O$ and 2.0 mmol $Fe(NO_3)_3 \cdot 9H_2O$ were dissolved in 32 ml distilled water (or water–ethanol mixed solvents). The mixture was stirred for 30 min and then 0.16 mol NaOH as a mineralizer was added to the above mixture. After being stirred for another 30 min, the mixture was transferred into a 40 ml Teflon-lined steel autoclave. The concentration of NaOH was 5 M. The volume percent of distilled water in the water–ethanol (H_2O–EtOH) mixed solvents was changed from 100% to 75%, 50%, 25% and 0%, and the samples synthesized in these solvents marked as S-100%, S-75%, S-50%, S-25% and S-0%, respectively (shown in Table 1). The autoclave was sealed and heated at 160 °C for 12 h and subsequently cooled to room temperature naturally. The products were collected using a centrifuge and then washed with water and ethanol several times. Finally, the samples were dried at 70 °C for 6 h.

The products were analyzed by an X-ray diffractometer (XRD, D/Max-RB, Rigaku, Japan) with a Cu Kα radiation in a 2θ range from 10° to 70°. The morphology of the product was examined by a scanning electron microscope (SEM, SSX-550, Shimadzu, Japan). Fourier transform infrared (FTIR) spectroscopy was performed with a spectrophotometer (Nicolet 67, Thermo, USA) with the KBr pellet technique. UV–vis diffuse reflectance spectra (DRS) of the samples were measured using $BaSO_4$ as a reference material by a UV–vis spectrophotometer (TU-1950, Beijing Perkinje General Instrument Co., Ltd, Beijing, China) with an integrating sphere. The photocatalytic activity of $Bi_2Fe_4O_9$ samples was evaluated under irradiation of a 400 W metal-halide lamp ($\lambda > 410$ nm) at natural pH value. The initial concentration of MO was 20 mg L^{-1} with a catalyst loading of 0.5 g L^{-1}. Before illumination, the solution was stirred for 30 min in the dark in order to reach the adsorption–desorption equilibrium between the photocatalyst and MO. At given intervals of illumination, a small quantity of the solution was taken, and the concentration of MO was determined by measuring the value at about 464 nm using a UV–vis spectrophotometer. Each time before the absorption measurement, the sample solution was centrifuged for 30 min to separate the catalyst powder from the solution. The absorption was converted to the MO concentration referring to a standard curve showing a linear behavior between the concentration and the absorption at this wavelength.

3. Results and discussion

3.1. Effect of solvent on phase structure and morphology

Fig. 1 shows the XRD patterns for the as-prepared powders synthesized in various solvents at 160 °C for 12 h. Obviously, all diffraction peaks in Fig. 1(a–d) can be indexed to a pure-phase $Bi_2Fe_4O_9$ with an orthorhombic crystal structure, keeping good consistency

Table 1
The synthesis conditions and optical-bandgaps of as-prepared $Bi_2Fe_4O_9$ products.

Sample	Water in water–ethanol mixed solvent (vol%)	Bandgap	Morphology
S-100%	100%	2.03 eV	rod
S-75%	75%	2.13 eV	cube
S-50%	50%	2.17 eV	defective cube
S-25%	25%	2.19 eV	defective cube
S-0%	0%	–	–

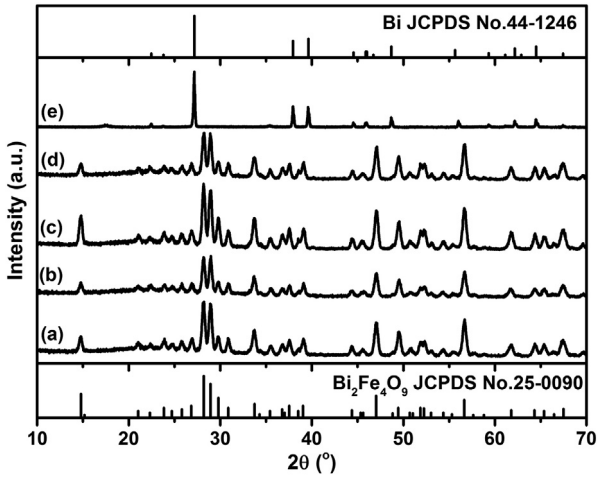

Fig. 1. XRD patterns of the as-prepared powders synthesized in the mixed solvents of H_2O and EtOH with different volume ratios at 160 °C for 12 h: (a) S-100%, (b) S-75%, (c) S-50%, (d) S-25% and (e) S-0%.

with the reported data (JCPDS card No. 25–0090). However, when EtOH was used as solvent, the synthesized sample was identified to be Bi, according to the powder data of JCPDS card No. 44–1246. This result demonstrated that pure-phase $Bi_2Fe_4O_9$ powders could not be obtained in the EtOH solvent. Because the dielectric constant of ethanol (24.3, 25 °C) was lower than that of water (78.3, 25 °C), the decrease in dielectric constant of the solvent tended to reduce the solubility of the reagent. As a result, it is hard for the chemical reaction to take place as ethanol was used as solvent such that there are no $Bi_2Fe_4O_9$ powders in the as-prepared products. Hence, water is critical for the synthesis of the $Bi_2Fe_4O_9$ phase under solvothermal conditions.

Fig. 2 shows the SEM images of the $Bi_2Fe_4O_9$ powders obtained in various solvents. It can be seen that the sample S-100% synthesized in distilled water exhibits well-defined rod-like shape, as shown in Fig. 2(a). Most of the rod-like crystals have a length of 2.5–3 μm, a thickness of 0.6 μm and a width ranging from 0.5 μm to 1.2 μm. As EtOH was introduced into the solvent, the sample S-75% (Fig. 2(b)) presents well-dispersed microcubes with rough faces and average edge length of ~1.2 μm. When the solvent in which H_2O and EtOH mixed in equal volume fraction was used, most of the $Bi_2Fe_4O_9$ crystals in the sample S-50% display a kind of defective morphology without obvious particle size change, as shown in Fig. 2(c). A groove-like defect could be observed in the cubic crystals. The defects in $Bi_2Fe_4O_9$ crystals become more obvious in the sample S-25% (Fig. 2(d)) with decreasing the percent of H_2O to 25% in the solvent. Two grooves can be observed in some crystals obviously. The results suggest that the morphology and size of $Bi_2Fe_4O_9$ crystals could be changed markedly by introducing a small amount of EtOH into the hydrothermal solvent. A large amount of EtOH tends to induce the formation of the defective crystal structures. In case of the sample S-75%, a mixture of EtOH and H_2O was used as solvent, which is less ionic than only H_2O used for the sample S-100%. Less ionic solvents are more likely to form more isotropic particle structures [18]. This might be the reason for the formation of cubic shaped particles in sample S-75%. Additionally, it can be seen from the SEM images that the crystal with defects is more prone to be obtained in case of using in H_2O–EtOH mixture as solvent. To investigate the possible formation mechanism of the rod-like $Bi_2Fe_4O_9$ crystals, time-dependent experiments were carried out. Products were collected at the reaction time of 3, 6, and 12 h, respectively. Their morphologies are shown in Figs. 3 and 2(a). After the hydrothermal treatment for 3 h, the product is composed of nanoparticles and microrods, and lots of nanoparticles are absorbed on the surface of the microrods, as shown in Fig. 3(a). When the reaction time was extended to 6 h,

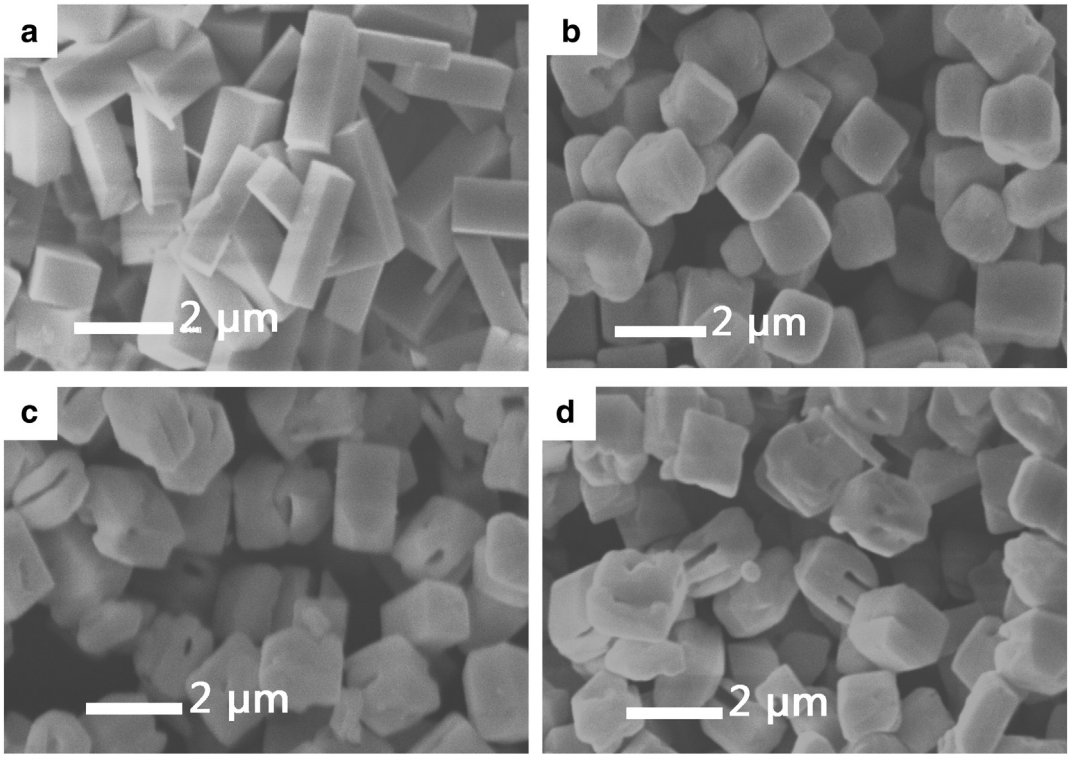

Fig. 2. SEM images of the as-prepared $Bi_2Fe_4O_9$ powders obtained in the mixed solvents of H_2O and EtOH with different volume ratios at 160 °C for 12 h: (a) S-100%, (b) S-75%, (c) S-50%, and (d) S-25%.

those microrods grow larger, as shown in Fig. 3(b). As the hydrothermal reaction time further increased to 12 h, only microrods could be observed in the products (Fig. 2(a)). On the basis of the above experimental results, it is suggested that the $Bi_2Fe_4O_9$ nanoparticles dissolve into the solution and grow onto the surface of larger $Bi_2Fe_4O_9$ crystals via a process known as Ostwald ripening. Moreover, the anisotropic nature of $Bi_2Fe_4O_9$ crystal structure might also contribute to the formation of rod-like crystals [19]. In addition, to investigate the formation of defects on $Bi_2Fe_4O_9$ microcrystals, the S-25% sample was taken as an example. A series of experiments with different reaction times were conducted, with each set corresponding to a different stage of the hydrothermal reaction. Fig. 4 shows the SEM morphology of the products at each stage. After hydrothermal treatment for 4 h, the product is composed of irregular aggregates and plate-like particles with cavity-like defects (Fig. 4(a)). By further prolonging the reaction time to 9 h, the aggregates are observed to disappear and most of the products are cubic shaped crystals with groove-like defects, accompanying with an increase of the thickness (Fig. 4(b)). When the reaction time was further increased to 12 h, there is no obvious change in the particle size and morphology, but it can be seen that the surface of the $Bi_2Fe_4O_9$ microcrystals becomes smoother (Fig. 2(d)). It is supposed that dissolution and Ostwald ripening process may dominate the crystal growth. Compared with water, the ethanol-containing solvent has low dielectric constant, in which saturation easily occurred and small crystallites may be steady. Therefore, the Ostwald ripening process was inhibited at the initial stage of hydrothermal process, which may result in the formation of $Bi_2Fe_4O_9$ particles with rough surface and some cavities (Fig. 4(a)). To minimize the overall energy of the system, these crystallites tend to aggregate. As the hydrothermal reaction continued, dissolution process occurred at the solid–liquid interfaces between the rough surface of aggregates and solvent. During the solid evacuation, the particles with defective morphology grow up at the expense of the smaller ones. As a result, the particle thickness increased and the rough surface of the $Bi_2Fe_4O_9$ particles became smooth as Ostwald ripening proceeding. In addition, the groove defects formed in the location of cavities when the dissolution proceeded.

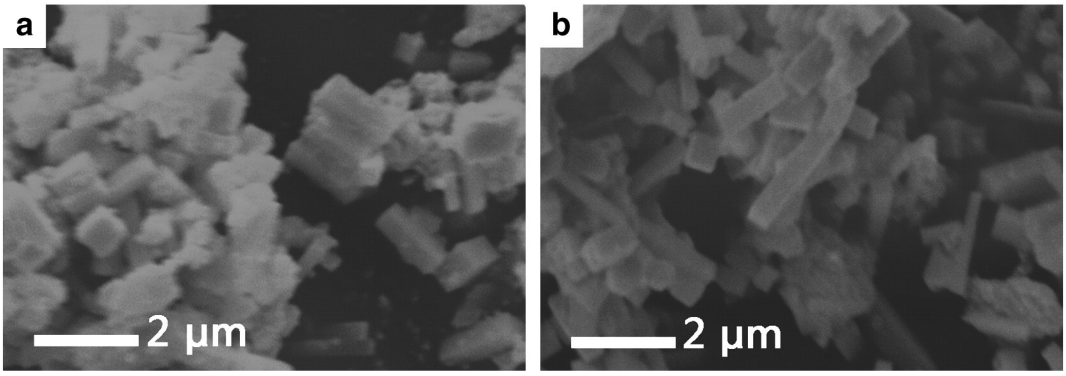

Fig. 3. SEM images of the $Bi_2Fe_4O_9$ samples (S-100%) synthesized in H_2O after (a) 3 h and (b) 6 h-hydrothermal treatment.

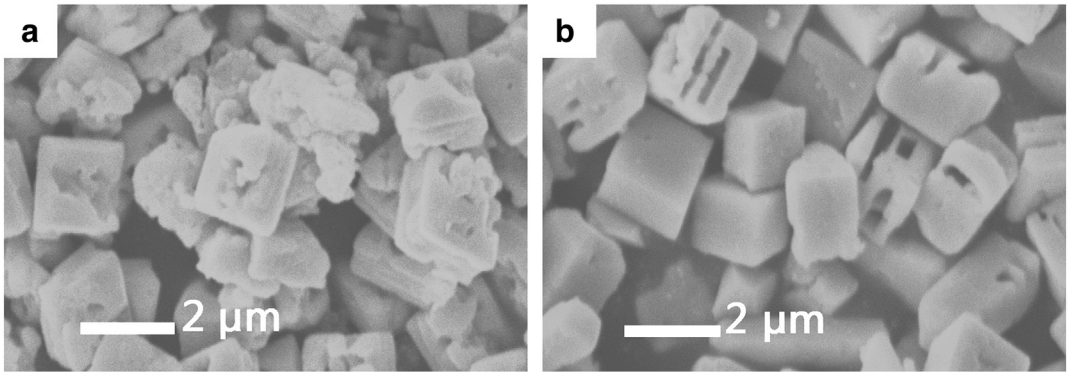

Fig. 4. SEM images of the $Bi_2Fe_4O_9$ samples (S-25%) synthesized in mixed H_2O/EtOH solvent after (a) 4 h and (b) 9 h-hydrothermal treatment.

3.2. FTIR analysis

The FTIR spectra of the $Bi_2Fe_4O_9$ samples synthesized in different solvents are shown in Fig. 5. The spectra are consistent with those previously reported [20]. The bands located at 400–813 cm^{-1} are attributed to the Fe–O stretching and bending vibration. There are two different sites for four iron atoms in the crystallographic structure of $Bi_2Fe_4O_9$: Fe_1 occupies a tetrahedral position and Fe_2 occupies an octahedral position. Its structure can be described by columns of edge-sharing $(Fe_2)O_6$ octahedra parallel to the c axis, linked by corner-sharing $(Fe_1)O_4$ tetrahedra and Bi atoms. The bands at 433 and 473 cm^{-1} are assigned to stretching vibrations of the FeO_6 octahedral. The bands at 541 and 578 cm^{-1} are attributed to the O–Fe–O and Fe–O–Fe bending vibration of the tetrahedral sites, respectively. The bands at 638 and 813 cm^{-1} are owing to the stretching vibration of the Fe cations in FeO_4 tetrahedra. It can be clearly seen that, when 25 vol% EtOH was introduced to the hydrothermal solvent, the bands at 541 and 578 cm^{-1} are shifted toward lower and higher wave-numbers, respectively. Accompanied by the obvious band shift, as the percent of EtOH in the hydrothermal solvent increases, the intensity of the band at 578 cm^{-1} has a little decrease. Besides, the band at 499 cm^{-1}, which is assigned to O–Fe–O bending vibration of the tetrahedral sites, becomes more intensified in the FTIR spectra as the percent of EtOH in mixed solvent increased. The band shift and intensity variation might be caused by the different morphology and size as well as the lattice distortions or defects in the crystal structure of the as-prepared $Bi_2Fe_4O_9$ microcrystals. The bands at 1384 cm^{-1} indicate the existence of nitrate ions. It can be seen that the sample S-75% has the strongest intensity. It is supposed that, compared with the sample S-100%, the sample S-75% could absorb more nitrate ions owing to the rough surface. However, with increasing the content of ethanol, the mixed solvent become less ionic, this can inhibit the adherence of the nitrate ion to the crystal. Therefore, the intensity of the band at 1384 cm^{-1} decreased gradually.

3.3. UV–vis analysis and photocatalytic performance

It is important to study the optical absorption of the as-prepared $Bi_2Fe_4O_9$ powders because the UV–vis absorption edge is relevant to the electronic structure feature and the energy band of the semiconductor catalyst. Fig. 6 shows the absorption spectra of the as-prepared $Bi_2Fe_4O_9$ samples transformed from the DRS spectra according to the Kubelka–Munk (K–M) theory [21]. The absorption spectra show that all $Bi_2Fe_4O_9$ samples can absorb considerable amounts of visible light, indicating their possibility of utilizing visible light for photocatalysis. Typically, there are two absorption edges: one is above 600 nm and another is above 800 nm. The former absorption can be ascribed to two types of excitations overlapped by each other. The first excitation process is due to the pair excitation processes: $^6A_{1g} + {}^6A_{1g} \rightarrow {}^4T_{1g}$ $(^4G) + {}^4T_{1g}$ (^4G) and the second one is caused by the excitation from $^6A_{1g}$ to ^4Eg, $^4A_{1g}$ (^4G) ligand field transitions (in octahedral coordination) and $^6A_1$ to $^4T_2$ (^4G) ligand field transitions (in tetrahedral coordination) as well as the charge-transfer band tail. The latter absorption results from the d–d electronic transitions of Fe [22,23]. The obvious shift in absorption edge may be due to the change of both morphology and particle size of the samples [24]. As discussed

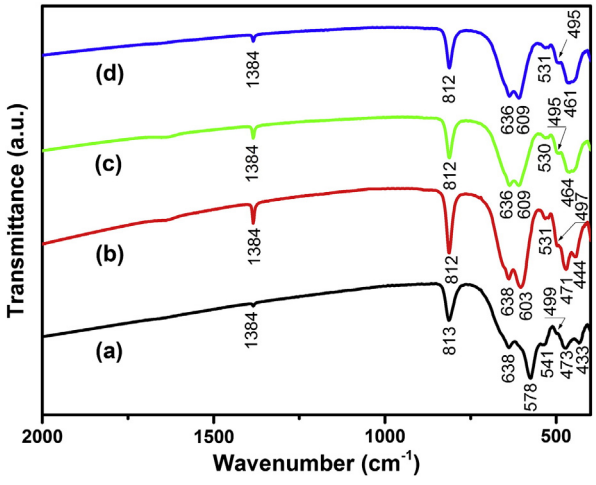

Fig. 5. FTIR spectra of the as-synthesized $Bi_2Fe_4O_9$ samples via a solvothermal method in mixed solvents of H_2O and EtOH with different volume ratios: (a) S-100%, (b) S-75%, (c) S-50%, and (d) S-25%.

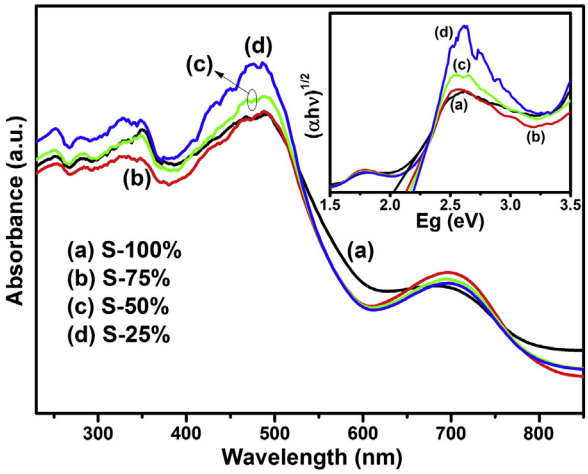

Fig. 6. UV–vis absorption spectra of the as-synthesized $Bi_2Fe_4O_9$ samples. The inset shows the square root of K–M functions ($\alpha h\nu$) versus photon energy.

above, the local crystal structure or bonding interactions change with varying shape and size (see Fig. 4). It is suggested that the change in the morphology of the as-prepared $Bi_2Fe_4O_9$ powders has strongly influenced the crystal field. And the transition shifts to higher or lower energy as the crystal field varied. Therefore, corresponding to the variation of the morphology, the change in the crystal structure strongly influences the optical absorption properties of $Bi_2Fe_4O_9$ samples. For a crystalline semiconductor, the optical absorption coefficient near the band edge follows the equation [25]

$$\alpha h\nu = A\left(h\nu - E_g\right)^{n/2}$$

where α, h, ν, E_g and A are absorption coefficient, Plank's constant, light frequency, band gap and a constant, respectively. The value of n is estimated to be 4, indicating an indirect transition of the $Bi_2Fe_4O_9$ samples. The band gap of $Bi_2Fe_4O_9$ can be calculated from the tangent line in the plot of the K–M function $((\alpha h\nu)^{1/2})$ vs photon energy (hν), as presented in the inset of Fig. 6. By extrapolating the tangent lines to $\alpha = 0$, the bandgaps of the $Bi_2Fe_4O_9$ samples S-100%, S-75%, S-50% and S-25% were estimated to be 2.03, 2.13, 2.17 and 2.19 eV, respectively (as shown in Table 1), which are comparable to those previously reported [5]. As discussed above, the variation of bandgap, i.e. the transition shift to higher or lower energy, was caused by the change of particle size and different particle morphology. These values indicate that $Bi_2Fe_4O_9$ is suitable for visible light photocatalysts.

Fig. 7 shows the photodegradation efficiencies of MO solution for as-prepared $Bi_2Fe_4O_9$ samples as a function of irradiation time under visible-light illumination. After 6 h visible-light irradiation without $Bi_2Fe_4O_9$ photocatalysts, the degradation rate of MO was less than 8%. It suggests that MO is stable under long-time visible-light irradiation if there is no photocatalyst involved. When the sample S-100% was used as photocatalyst, after the visible-light irradiation for 6 h, the MO degradation rate is about 15%. In contrast, samples S-75%, S-50% and S-25% exhibit a higher potocatalytic activity. About 29%, 31% and 33% MO were degraded by these samples under the same experimental condition, respectively. The difference in degradation rate under the same condition could be attributed to the following reasons. Firstly, it is known that, only the electron–hole pairs on photocatalyst surface can react with adsorbed organic reactants as a redox source, finally leading to the decomposition of the organic reactants [26]. However, the degradation of the absorbed organic is usually inhibited by the recombination of the electron–hole pairs in this process. For these photo-generated charge carriers, the average diffusion time (τ) from bulk to surface follows the equation

$$\tau = r^2\pi^2 D^2$$

where r is the grain radius and D is the diffusion coefficient of the carrier [27]. With increasing the size of the $Bi_2Fe_4O_9$ powders, the electron–hole pairs will take a longer time to diffuse to the photocatalyst surface. Therefore, the recombination of electron–hole pairs is more likely to occur during the electron–hole diffusion, and result in the degradation of photocatalytic activity. Smaller $Bi_2Fe_4O_9$ crystals have larger specific surface areas, meaning that they could possess more reactive sites and higher photon absorption rates on the surface. This is also helpful to the higher photodegradation rates. In addition, the bandgaps of cubic-shaped $Bi_2Fe_4O_9$ samples (2.13, 2.17 and 2.19 eV) are wider than those of rod-like $Bi_2Fe_4O_9$ samples (2.03 eV). $Bi_2Fe_4O_9$ microcubes with wider bandgaps provide stronger oxidation performance. All of the above factors result in the lowest photocatalytic activity of the sample S-100%.

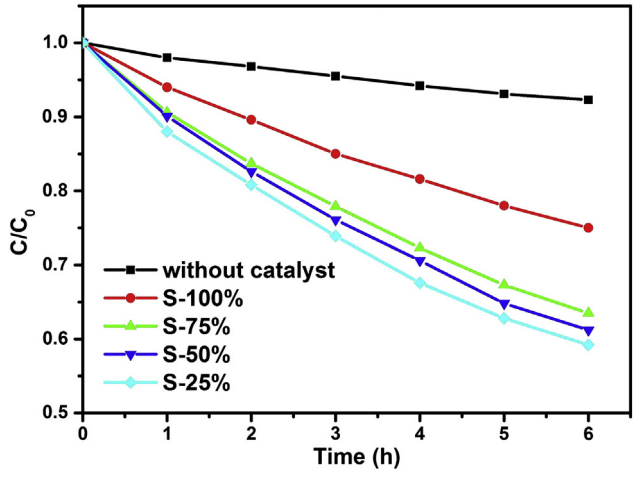

Fig. 7. The photocatalysis of the as-prepared $Bi_2Fe_4O_9$ samples on degradation of MO under visible light irradiation.

4. Conclusions

In the present work, pure $Bi_2Fe_4O_9$ powders were successfully synthesized by using a surfactant-free solvothermal route in H_2O–EtOH mixed solvents. The morphology and particle size could be easily tuned by varying the volume ratios of H_2O/EtOH. Rod-like and cubic shape crystals were obtained in H_2O and H_2O–EtOH mixed solvents, respectively. The microrods were formed by a typical Ostwald ripening process. The groove-like defects on the $Bi_2Fe_4O_9$ crystals synthesized in H_2O/EtOH mixed solvent may form as a result of the dissolution process. The optical property and photocatalytic performance of the as-prepared $Bi_2Fe_4O_9$ crystals were discussed carefully as well.

Acknowledgments

This work was financially supported by a project of Natural Science Foundation of Anhui Province (1108085J14), and the National Natural Science Foundation of China (51272060).

References

[1] J. Wang, J.B. Neaton, H. Zheng, V. Nagarajan, S.B. Ogale, B. Liu, D. Viehland, V. Vaithyanathan, D.G. Schlom, U.V. Waghmare, N.A. Spaldin, K.M. Rabe, M. Wuttig, R. Ramesh, Epitaxial $BiFeO_3$ multiferroic thin film heterostructures, Science 299 (2003) 1719–1722.
[2] M. Valant, D. Suvorov, A stoichiometric model for sillenites, Chem. Mater. 14 (2002) 3471–3476.
[3] A.S. Poghossian, H.V. Abovian, P.B. Avakian, S.H. Mkrtchian, V.M. Haroutunian, Bismuth ferrites: new materials for semiconductor gas sensors, Sensors Actuators B 4 (1991) 545–549.
[4] A.K. Singh, S.D. Kaushik, B. Kumar, P.K. Mishra, A. Venimadhav, V. Siruguri, S. Patnaik, Substantial magnetoelectric coupling near room temperature in $Bi_2Fe_4O_9$, Appl. Phys. Lett. 92 (2008) 132910.
[5] Q.J. Ruan, W.D. Zhang, Tunable morphology of $Bi_2Fe_4O_9$ crystals for photocatalytic oxidation, J. Phys. Chem. C 113 (2009) 4168–4173.
[6] S.M. Sun, W.Z. Wang, L. Zhang, M. Shang, Visible light-induced photocatalytic oxidation of phenol and aqueous ammonia in flowerlike $Bi_2Fe_4O_9$ suspensions, J. Phys. Chem. C 113 (2009) 12826–12831.
[7] N.I. Zakharchenko, Catalytic properties of the Fe_2O_3–Bi_2O_3 system in ammonia oxidation to nitrogen oxides, Kinet. Catal. 43 (2002) 95–98.
[8] Z. Yang, Y. Huang, B. Dong, H.L. Li, S.Q. Shi, Densely packed single-crystal $Bi_2Fe_4O_9$ nanowires fabricated from a template-induced sol–gel route, J. Solid State Chem. 179 (2006) 3324–3329.
[9] T.J. Park, G.C. Papaefthymiou, A.R. Moodenbaugh, Y. Mao, S.S. Wong, Synthesis and characterization of submicron single-crystalline $Bi_2Fe_4O_9$ cubes, J. Mater. Chem. 15 (2005) 2099–2105.
[10] Y. Xiong, M. Wu, Z. Peng, N. Jiang, Q. Chen, Hydrothermal synthesis and characterization of $Bi_2Fe_4O_9$ nanoparticles, Chem. Lett. 33 (2004) 502–503.
[11] X.Y. Zhang, L. Bourgeois, J.F. Yao, H.T. Wang, P.A. Webley, Tuning the morphology of bismuth ferrite nano- and microcrystals: from sheets to fibers, Small 3 (2007) 1523–1528.
[12] J.T. Han, Y.H. Huang, R.J. Jia, G.C. Shan, R.Q. Guo, W. Huang, Synthesis and magnetic property of submicron $Bi_2Fe_4O_9$, J. Cryst. Growth 294 (2006) 469–473.

[13] Y. Du, Z. Cheng, S. Dou, X. Wang, Tunable morphology and magnetic properties of $Bi_2Fe_4O_9$ nanocrystal synthesized by hydrothermal method, J. Nanosci. Nanotechnol. 11 (2011) 2691–2695.
[14] K. Byrappa, M. Yoshimura, Handbook of Hydrothermal Technology, William Andrew Inc, Norwich, New York, 2001.
[15] Y.C. Zhu, T. Mei, Y. Wang, Y.T. Qian, Formation and morphology control of nanoparticles via solution routes in an autoclave, J. Mater. Chem. 21 (2011) 11457–11463.
[16] S.G. Kwon, B.H. Park, K. Choi, E.S. Choi, S. Nam, J.W. Kim, J.H. Kim, Solvothermally synthesized tetragonal barium titanate powders using H_2O/EtOH solvent, J. Eur. Ceram. Soc. 26 (2006) 1401–1404.
[17] N. Wei, D.M. Zhang, X.Y. Han, F.X. Yang, Z.C. Zhong, K.Y. Zheng, Synthesis and mechanism of ferroelectric potassium tantalate niobate nanoparticles by the solvothermal and hydrothermal processes, J. Am. Ceram. Soc. 90 (2007) 1434–1437.
[18] A. Chaudhuri, S. Mitra, M. Mandal, K. Mandal, Nanostructured bismuth ferrites synthesized by solvothermal process, J. Alloys Compd. 491 (2010) 703–706.
[19] N. Niizeki, M. Wachi, The crystal structures of $Bi_2Mn_4O_{10}$, $Bi_2Al_4O_9$ and $Bi_2Fe_4O_9$, Z. Kristallogr. 127 (1968) 173–187.
[20] D. Voll, A. Beran, H. Schneider, Variation of infrared absorption spectra in the system $Bi_2Al_{4-x}Fe_xO_9$ ($x = 0$–4), structurally related to mullite, Phys. Chem. Miner. 33 (2006) 623–628.
[21] P. Kubelka, F. Munk, Ein beitrag zur optik der farbanstriche, Z. Tech. Phys. 12 (1931) 593–601.
[22] D.M. Sherman, The electronic structures of Fe^{3+} coordination sites in iron oxides: applications to spectra, bonding, and magnetism, Phys. Chem. Miner. 12 (1985) 161–175.
[23] Y.P. He, Y.M. Miao, C.R. Li, S.Q. Wang, L. Cao, S.S. Xie, G.Z. Yang, B.S. Zou, C. Burda, Size and structure effect on optical transitions of iron oxide nanocrystals, Phys. Rev. B 71 (2005) 125411.
[24] G. Zhou, M. Lü, F. Gu, S. Wang, Z. Xiu, X. Cheng, Controlled synthesis and optical properties of $PbCrO_4$ nanorods and nanoparticles, J. Cryst. Growth 270 (2004) 283–287.
[25] M.A. Butler, Photoelectrolysis and physical properties of the semiconducting electrode WO_2, J. Appl. Phys. 48 (1977) 1914–1920.
[26] M.R. Hoffmann, S.T. Martin, W. Choi, D.W. Bahnemann, Environmental applications of semiconductor photocatalysis, Chem. Rev. 95 (1995) 69–96.
[27] M. Shang, W.Z. Wang, S.M. Sun, L. Zhou, L. Zhang, Bi_2WO_6 nanocrystals with high photocatalytic activities under visible light, J. Phys. Chem. C 112 (2008) 10407–10411.